








RESEARCH ARTICLE | JUNE 20 2024

## Demonstrating grating-based phase-contrast imaging of laser-driven shock waves

Leonard Wegert  ; Stephan Schreiner ; Constantin Rauch ; Bruno Albertazzi; Paulina Bleuel ; Eric Fröjdh ; Michel Koenig ; Veronika Ludwig ; Artem S. Martynenko ; Pascal Meyer ; Aldo Mozzanica ; Michael Müller ; Paul Neumayer ; Markus Schneider ; Angelos Triantafyllidis ; Bernhard Zielbauer ; Gisela Anton ; Thilo Michel ; Stefan Funk 

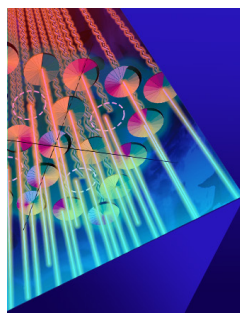


*Matter Radiat. Extremes* 9, 047803 (2024)

<https://doi.org/10.1063/5.0200440>



 AIP  
Publishing



Matter and Radiation  
at Extremes

Special Topics Now Online

[Read Now](#)

 AIP  
Publishing 

Featured

# Demonstrating grating-based phase-contrast imaging of laser-driven shock waves

Cite as: Matter Radiat. Extremes 9, 047803 (2024); doi: 10.1063/5.0200440

Submitted: 26 January 2024 • Accepted: 20 May 2024 •

Published Online: 20 June 2024



View Online



Export Citation



CrossMark

Leonard Wegert,<sup>1,a)</sup> Stephan Schreiner,<sup>2</sup> Constantin Rauch,<sup>2</sup> Bruno Albertazzi,<sup>3</sup> Paulina Bleuel,<sup>2</sup> Eric Fröjdh,<sup>4</sup> Michel Koenig,<sup>3</sup> Veronika Ludwig,<sup>2</sup> Artem S. Martynenko,<sup>1</sup> Pascal Meyer,<sup>5</sup> Aldo Mozzanica,<sup>4</sup> Michael Müller,<sup>2</sup> Paul Neumayer,<sup>1</sup> Markus Schneider,<sup>2</sup> Angelos Triantafyllidis,<sup>3</sup> Bernhard Zielbauer,<sup>1</sup> Gisela Anton,<sup>2</sup> Thilo Michel,<sup>2</sup> and Stefan Funk<sup>2</sup>

## AFFILIATIONS

<sup>1</sup> Plasma Physics Department, GSI Helmholtzzentrum für Schwerionenforschung, Planckstraße 1, 64291 Darmstadt, Germany

<sup>2</sup> Erlangen Centre for Astroparticle Physics (ECAP), Friedrich-Alexander-Universität Erlangen-Nürnberg, Nikolaus-Fiebiger-Straße 2, 91058 Erlangen, Germany

<sup>3</sup> LULI-CNRS, CEA, Sorbonne Universités, École Polytechnique, Institut Polytechnique de Paris, F-91120 Palaiseau Cedex, France

<sup>4</sup> Paul Scherrer Institut (PSI), Forschungsstrasse 111, 5232 Villigen, Switzerland

<sup>5</sup> Karlsruhe Institute of Technology, Institute of Microstructure Technology, Hermann-von-Helmholtz-Platz 1, 76344 Eggenstein-Leopoldshafen, Germany

<sup>a)</sup> Author to whom correspondence should be addressed: [L.Wegert@gsi.de](mailto:L.Wegert@gsi.de)

## ABSTRACT

Single-shot X-ray phase-contrast imaging is used to take high-resolution images of laser-driven strong shock waves. Employing a two-grating Talbot interferometer, we successfully acquire standard absorption, differential phase-contrast, and dark-field images of the shocked target. Good agreement is demonstrated between experimental data and the results of two-dimensional radiation hydrodynamics simulations of the laser-plasma interaction. The main sources of image noise are identified through a thorough assessment of the interferometer's performance. The acquired images demonstrate that grating-based phase-contrast imaging is a powerful diagnostic tool for high-energy-density science. In addition, we make a novel attempt at using the dark-field image as a signal modality of Talbot interferometry to identify the microstructure of a foam target.

© 2024 Author(s). All article content, except where otherwise noted, is licensed under a Creative Commons Attribution (CC BY) license (<http://creativecommons.org/licenses/by/4.0/>). <https://doi.org/10.1063/5.0200440>

## I. INTRODUCTION

X-ray radiography is an established diagnostic tool in high-energy-density (HED) physics.<sup>1</sup> Its applications range from equation-of-state measurements in dense plasmas,<sup>2,3</sup> to laboratory astrophysics,<sup>4-7</sup> to inertial confinement fusion (ICF).<sup>8</sup> Typically, these methods involve measuring X-ray transmission through the target under study, probing the complex part  $\beta$  of the target's refractive index  $n = 1 - \delta + i\beta$ . In a simple absorption imaging setup, the phase shift, caused by the real part  $\delta$  of the refractive index, is usually not measured. X-ray phase-contrast imaging is capable of additionally measuring  $\delta$ , providing information directly proportional to the

electron density of the material.<sup>9</sup> This technique has the potential to enhance discrimination between weakly absorbing materials. It facilitates the detection of small density changes, making it a promising tool for HED research.<sup>10</sup>

Currently, HED experiments mainly employ propagation-based phase-contrast imaging. This technique relies on the spatial propagation of the altered phase front, imposing high demands on the spatial coherence of the X-ray source. As a result, this technique finds primary application at free-electron laser (FEL) facilities,<sup>11,12</sup> but has also been demonstrated with laser-driven backlights.<sup>13,14</sup> Grating-based phase-contrast imaging uses a grating interferometer to obtain phase information. A three-grating configuration, also

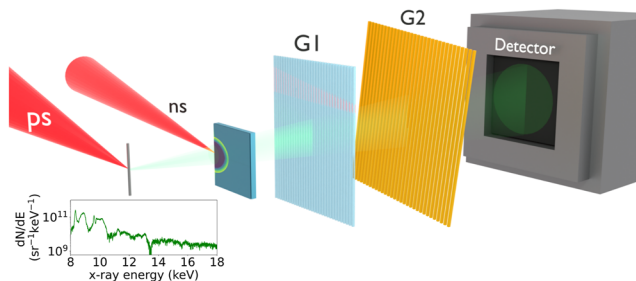


**FIG. 1.** Schematic of experimental setup for X-ray Talbot interferometry of laser-driven shock waves. A ps laser pulse is focused on a thin wire to produce X-rays that propagate through the target of interest, which has previously been irradiated with a ns laser beam. The Talbot interferometer, placed downstream of the target, is formed by the gratings  $G_1$  and  $G_2$ . Finally, the X-rays are detected by a digital detector protected from electromagnetic pulses by a Faraday cage.<sup>23</sup> Note that an 8 cm-long deflecting magnet (0.5 T), placed in front of the grating  $G_1$ , is not shown. The inset shows an example of the spectrum of a 5  $\mu\text{m}$  tungsten wire measured at PHELIX in the range from 8 to 18 keV. See the [supplementary material](#) for an enlarged version.

referred to as Talbot–Lau deflectometry, can be used with X-ray sources of large spatial extent, utilizing a source grating to divide the incoherent source into several individually coherent ones.<sup>15</sup> This approach has already been used for experiments with laser-driven X-ray sources.<sup>16,17</sup>

However, the implementation of a three-grating configuration requires the use of an absorptive source grating, which reduces the photon flux. The close proximity to the backlighter often results in damage to this grating. By omitting the source grating, the need for its frequent replacement can be avoided entirely. Further, the already limited photon flux will not be additionally reduced. This adaption is only possible when an X-ray source with a focal spot size in the micrometer range is employed to ensure sufficient spatial coherence.<sup>18</sup> In two beamtimes at the PHELIX facility in 2019 and 2020, we successfully demonstrated this approach on static test samples.<sup>19–21</sup> Since then, we have further improved our setup.

In this paper, we present results on imaging laser-driven shock waves with grating-based phase-contrast imaging obtained at the PHELIX and LULI2000 laser facilities. The results are compared with radiation hydrodynamics simulations using the code FLASH<sup>22</sup> to qualitatively verify our findings.

## II. IMAGING SETUP AND METHOD

In this paper, a grating interferometer, also referred to as a Talbot interferometer,<sup>18–21,24–27</sup> consisting of two microstructured gratings and an X-ray detector, is used in combination with a laser-driven X-ray source of high spatial coherence (see Fig. 1).

We apply phase-contrast imaging to image laser-driven shock waves in plastic targets, both at solid density and in the form of low-density foam. The strong shock waves are driven by the hot plasma produced upon irradiation with energetic laser pulses, a common technique to generate Mbar pressures. Detailed descriptions of the shocked targets are available in Secs. III A and III B

for the experiments conducted at the PHELIX and LULI facilities, respectively. The setup of the Talbot imaging system, shown in Fig. 1, is similar to the standard setup for absorption imaging in the point projection scheme. The object to be imaged is placed between a small X-ray source and an X-ray detector, a configuration that projects a magnified image of the object onto the detector itself. We use a digital JUNGFRÄU detector, a hybrid pixel detector developed by the Paul Scherrer Institute (PSI). This is a charge-integrating detector, with single-photon sensitivity and wide dynamic range thanks to the automatic gain architecture.<sup>28</sup> The three gains are factory-calibrated so that the recorded signal can be given in terms of the X-ray energy deposited in each pixel. The detector has a pixel pitch of 75  $\mu\text{m}$ , a pixel count of 1 Mpx and a frame rate of 2 kHz. To shield the detector from the strong electromagnetic pulses produced during short-pulse laser–matter interactions,<sup>29</sup> a housing specifically designed for protection from such pulses<sup>23</sup> is employed. Additionally, for grating-based phase-contrast imaging, two microstructured gratings are placed between the object and the detector. These gratings were fabricated by the Institute of Microstructure Technology (IMT/KIT) using deep X-ray lithography.<sup>30</sup>

Grating-based phase-contrast imaging exploits the Talbot effect<sup>31</sup> to retrieve the phase shift induced by the object. When a coherent source illuminates a periodic structure such as a grating, self-images of the structure appear downstream at specific distances.<sup>32</sup> An object placed in the beam alters the phase front, which causes the self-image to shift. Hence, the phase shift of the target is encoded in the shift of the self-image. Since most X-ray detectors are unable to spatially resolve the self-image of the grating, a second grating ( $G_2$ ) is placed toward the detector. This superposition of two periodic structures creates a Moiré pattern with a period large enough to be resolvable by the detector.<sup>33</sup> The pattern’s contrast, termed the fringe visibility  $V$ , follows the definition of the Michelson contrast<sup>9</sup> and is calculated using

$$V = \frac{\tilde{I}_{\max} - \tilde{I}_{\min}}{\tilde{I}_{\max} + \tilde{I}_{\min}}, \quad (1)$$

with  $\tilde{I}_{\max}$  and  $\tilde{I}_{\min}$  denoting the maximum and minimum intensities.

To extract the relevant information, a reference measurement with no object has to be used in addition to the object measurement. The phase information, encoded in the Moiré fringe pattern, is separated from the transmission information in Fourier space for both object and reference image. The differential phase-contrast (DPC) signal is then defined as the phase difference between the periodic pattern of the object and the periodic pattern. The dark-field image (DF) quantifies the ratio of the fringe visibilities in the object and reference measurements and is a measure of small-angle scattering and object boundaries.<sup>34</sup> In this paper, the processing of raw detector images is based on the work of Takeda *et al.*<sup>35</sup> and Bennett *et al.*,<sup>36</sup> incorporating the modifications suggested by Seifert *et al.*<sup>37</sup>

To obtain high-quality phase-contrast images, the grating interferometer must be optimized for the investigated sample. For the Talbot interferometer used here, the grating parameters and geometry were optimized with respect to the minimal detectable refraction

angle  $\alpha_{\min}$ , which is a measure of the sensitivity to the X-ray refraction caused by the object.<sup>38,39</sup> The optimization process of the imaging setup is described in detail by Schreiner *et al.*<sup>40</sup>

As the Talbot interferometer requires a high spatial coherence, the X-ray source size has to be small. This is also required to achieve a sufficient spatial resolution for the expected feature sizes of the object under investigation. To enable single-exposure images with an acceptable image noise, a high yield in the required photon energy range is necessary. Finally, given the rapid hydrodynamic evolution of samples under HED conditions, the X-ray emission should be short-lived, ideally of order 10 ps, to avoid motion blurring. To realize the X-ray source, we employ energetic laser pulses with a duration of a few picoseconds, focused to relativistic intensities onto a 5  $\mu\text{m}$ -diameter tungsten wire.<sup>41</sup> Achieving relativistic intensities, the intense laser-matter interaction produces copious amounts of superthermal electrons, with energies ranging up to several hundred keV. Their propagation through the backlighter wire generates intense emission of energetic bremsstrahlung and inner-shell X-ray fluorescence.

### III. EXPERIMENTAL DETAILS AND RESULTS

In the following, results from beamtimes at the PHELIX and LULI2000 laser facilities are presented with the aim of showcasing the capabilities of grating-based phase-contrast imaging using laser driven X-ray sources.

#### A. PHELIX

The experiment was performed at the GSI Helmholtz Center for Heavy Ion Research in Germany using the PHELIX Nd:glass laser ( $\lambda = 1054 \text{ nm}$ ).<sup>42</sup> The 7 ns-long driver beam with 30 J of laser energy launched a shock wave into an aluminum flash-coated polymethyl methacrylate (PMMA) target. With  $\sim 50\%$  of the pulse energy in the main focal spot of 17  $\mu\text{m}$  full width at half maximum (FWHM), as indicated by focus measurements, this resulted in an on-target intensity of  $0.7 \times 10^{15} \text{ W/cm}^2$ . After a delay of 9.5 ns, a second laser beam, also carrying 30 J, with a duration of 8 ps was focused down to a spot size of  $\sim 5 \mu\text{m}$  FWHM and hit a 5  $\mu\text{m}$  thin tungsten wire.

Optimizing the grating parameters and modeling of the final images requires knowledge of the emitted X-ray spectrum. Hence, we measured the X-ray backlighter spectrum in the energy range from 8 to 18 keV using a highly oriented pyrolytic graphite (HOPG) spectrometer in von-Hamos geometry. See the [supplementary material](#) for a measured tungsten spectrum.

Optimization of the gratings in preparation for the beamtime resulted in the grating parameters and geometry given in [Table I](#). An example of a raw image taken at the PHELIX facility with the designed setup is shown in [Fig. 2\(a\)](#), where the color code represents the deposited energy in keV. The Moiré pattern is arranged horizontally with a slight counter-clockwise rotation. In addition, a vertical structure is present, which is caused by microfractures in the grating  $G_2$ . These defects stemmed from the graphite wafer used as the substrate. [Figure 2\(c\)](#) shows an example of a lineout generated from the pixels highlighted in red in [Fig. 2\(a\)](#). The Moiré pattern has an average visibility of  $15\% \pm 3\%$ . Since the fringe displacement is used to measure the phase shift, the spatial resolution of the phase

**TABLE I.** Parameters of imaging setup used at the PHELIX facility. The thickness of the grating  $G_1$  was chosen such that it was  $\pi$ -shifting for 11 keV. The duty cycle (DC) is the ratio of the grating bar width to the period. The grating  $G_1$  was fabricated on a 500  $\mu\text{m}$  polyimide wafer and the grating  $G_2$  on a 200  $\mu\text{m}$  graphite wafer.

	Position (mm)	Period ( $\mu\text{m}$ )	Height ( $\mu\text{m}$ )	Material	DC
Target	30				
$G_1$	300	10.6	30	SU8	0.5
$G_2$	538	9.5	95	Au	0.66
Detector	930				

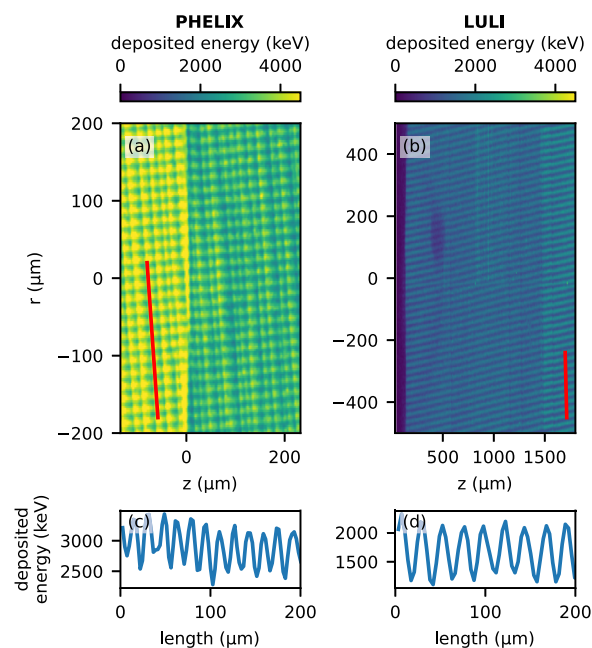


**FIG. 2.** Moiré fringe patterns obtained at PHELIX (a) and LULI (b). The color code is the same for both images and indicates the deposited X-ray energy in keV. The axis indicates the spatial extent in the object plane. Vertical red lines in the images mark the pixels from which the lineouts in (c) and (d) were generated. The fringe visibilities obtained at the PHELIX and LULI lasers were  $15\% \pm 3\%$  and  $28\% \pm 3\%$ , respectively. Note that the vertical stripes in the image obtained at PHELIX stem from defects in the absorption grating used.

shift is limited by the fringe spacing.<sup>35</sup> Hence, to obtain good spatial resolution in the differential phase-contrast, a Moiré period of about 6.5 pixels was chosen. Considering the magnification of the target plane into the detector plane of about 31 and the pixel size of 75  $\mu\text{m}$ , one fringe period spans over 16  $\mu\text{m}$  in the target plane. This makes the spatial resolution of the DPC worse compared with the transmission image, because the latter is limited by the X-ray source size.

The retrieved transmission and differential phase-contrast images from the object measurement presented in [Fig. 2\(a\)](#) are



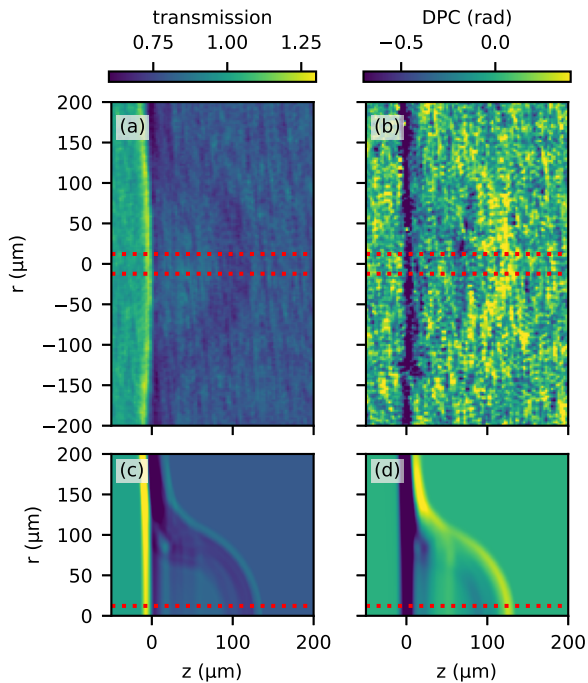


**FIG. 3.** Retrieved transmission image (a) and differential phase-contrast image (b) from data acquired at the PHELIX laser. The  $23\ \mu\text{m}$  wide areas (10 pixels) marked by the red dashed lines are used to generate the lineouts plotted in Fig. 4. The expected density distribution is simulated with FLASH and shown in (c) and (d). Because of the cylindrical nature of the experiment, only half of each simulated image is displayed.

shown in Figs. 3(a) and 3(b), respectively. The target is clearly visible in the transmission image at  $z \geq 0$ , since the  $0.5\ \text{mm}$  of PMMA absorbed a significant amount of X-ray photons. Further, edge enhancement on the target edge due to propagation-based phase-contrast is noticeable. The shock front, visible as a darker half-sphere inside the target, has propagated about  $130\ \mu\text{m}$  into the material. It is also visible in the DPC image, where the strong density gradient at the shock front produces a phase shift of  $\sim 0.2\ \text{rad}$ . Since grating-based phase-contrast imaging is only sensitive perpendicular to the vertically aligned grating bars, the signal from the shock front becomes weaker where it extends in the vertical direction. Both transmission and DPC images suffer from the source size of  $\sim 30\ \mu\text{m}$  in the vertical direction, owing to the orientation of the backlighter wire. Also clearly noticeable is the noise in the retrieved transmission and DPC images, which strongly affects the data quality. A significant contributor is the microfractured grating  $G_2$ . The noise stemming from this source is nonstatistical and shows a periodicity of about nine pixels. In the DPC image, the noise appears as locally confined areas with a slight offset compared with the expected DPC values. A further contributor to the image noise is the limited photon flux from the X-ray backlighter.

We performed 2D radiation hydrodynamics simulations using the FLASH code to benchmark the measurement results. These simulations were performed in a cylindrical symmetric geometry

and with a maximum resolution of  $250\ \text{nm}$ . SESAME Table 7740 for polycarbonate<sup>43</sup> was used as the material's equation of state. Its opacities were generated with the multigroup opacity code TOPS.<sup>44</sup> Consistent with focus images taken during the beamtime, the focal spot of the driver laser was modeled as a main focal spot with a Gaussian intensity distribution with  $17\ \mu\text{m}$  FWHM, together with a larger  $80\ \mu\text{m}$  FWHM spot at lower intensity. Only about 20% of the laser energy measured during the experiment was needed to match the propagation of the shock front in the simulations to the experimental results. A possible reason for this discrepancy might be the high intensity of about  $0.7 \times 10^{15}\ \text{W}/\text{cm}^2$  and the long wavelength of the laser driving the shock wave. In this regime, the amount of laser absorption via inverse bremsstrahlung can be decreased by more than 50% owing to the high quiver velocity of the electrons in the laser electric field. Furthermore, parametric instabilities start to become noticeable, leading to significant backscatter through, for example, stimulated Brillouin and Raman scattering.<sup>45</sup> The FLASH simulations only considered inverse bremsstrahlung and did not take parametric instabilities into account. Therefore, in the simulations, a lower laser energy was used to model a realistic amount of laser energy coupling to the plasma.

To compare the results from the radiation hydrodynamics simulations with the retrieved image modalities from the experiment, the simulated data were post-processed. To incorporate the propagation effects in the transmission image, an incoherent X-ray source illumination was assumed.<sup>46</sup> The differential phase-contrast image was calculated using the relation between the density distribution of the target and the expected phase-contrast signal given by Engelhardt *et al.*<sup>25</sup> The final results are presented in the lower half of Fig. 3.

For a quantitative comparison between the simulation and the experimental data, lineouts were calculated within the red dashed lines in Fig. 3. The results are shown in Figs. 4(a) and 4(b) for the transmission and differential phase-contrast images, respectively. The blue crosses are the column-wise averaged values of ten detector pixels. To account for the vertical defects of the grating  $G_2$ , we applied a sliding average window of three pixels in the  $z$  direction for the transmission signal and six pixels for the DPC signal. The results are shown by the dark blue lines. The light blue bands indicate the estimated standard deviations. Since the nonstatistical noise from the grating defects makes a simple error estimation approach infeasible, the standard deviation of a region where no object was present was used as an estimate for image noise. For different positions in the grating, we obtain on average standard deviations of  $0.017$  and  $0.12\ \text{rad}$  for the transmission and differential phase-contrast images, respectively. The signal from the simulation is shown in red.

Overall, the simulations agree reasonably well with the experimental signals. The greatest difference is in the signal amplitude of the target's edge at  $z = 0$  in the DPC image. A possible reason for the discrepancy is a lack of spatial resolution in the DPC signal, resulting from the Moiré fringe period of  $16\ \mu\text{m}$ . Rapidly changing density gradients, such as those present at the target edge, will be smeared out in the DPC signal. Furthermore, the applied sliding average algorithm acts as a low-pass filter and thus decreases the amplitude for sharp-edged signals. More discrepancies emerge in the area between  $50\ \mu\text{m}$  and the shock front at about  $125\ \mu\text{m}$ . The

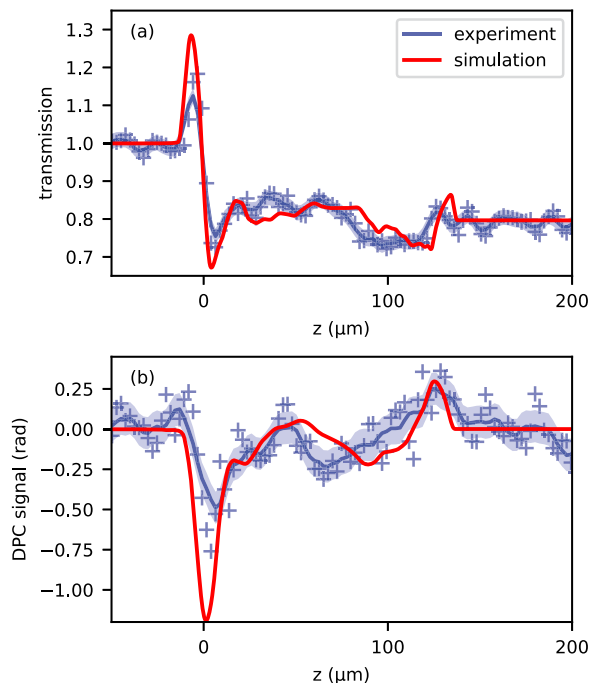


**FIG. 4.** Lineouts from the areas marked in red in Fig. 3 averaged along the  $r$  axis: (a) transmission image; (b) differential phase-contrast image. The red lines are obtained from the simulated images and the blue crosses from the data obtained in the experiment. The light blue bands indicate the standard deviation of the data. The dark blue lines show the data along the  $z$  direction smoothed.

discrepancies appear to be more pronounced in the phase-contrast signal. This highlights the advantage of having an extra signal in addition to the transmission image.

### B. LULI

At the LULI2000 laser facility (École Polytechnique, Palaiseau, France), we used the PICO2000 beam to irradiate a  $5\ \mu\text{m}$ -thick tungsten backlighter wire with laser pulses at  $\sim 100\ \text{J}$  and pulse durations of  $1\ \text{ps}$ , focused to a spot size of roughly  $15\ \mu\text{m}$ . The NANO2000 beam of the facility was used to irradiate a  $20\ \mu\text{m}$ -thick plastic ablator from a foam target of density  $0.25\ \text{g}/\text{cm}^3$ . The laser pulse carried  $200\ \text{J}$  energy in a flat-top pulse of  $1.5\ \text{ns}$  duration at  $527\ \text{nm}$ . We employed a phase plate to produce an approximately constant intensity over a diameter of  $500\ \mu\text{m}$ , yielding a nominal intensity of  $7 \times 10^{13}\ \text{W}/\text{cm}^2$ . According to our simulations, the shock wave should be nearly planar in the first few nanoseconds after the laser irradiation, before becoming spherical. A copper flag was used to shield the detector from the preplasma emission. The data presented here show the shock wave after  $30\ \text{ns}$ .

Using the tungsten spectrum measured during the PHELIX experiment, we fine-tuned our grating interferometer. The thickness of the grating  $G_1$  bars was chosen to be  $\pi$ -shifting at  $10\ \text{keV}$  and the grating positions were adjusted accordingly. For the grating  $G_2$ , we switched from a graphite to a polyimide wafer to prevent microfractures. The new parameters are listed in Table II. These changes nearly doubled the fringe visibility, to  $28\% \pm 3\%$ . The raw

**TABLE II.** Parameters of the imaging setup used at the LULI facility. The thickness of the grating  $G_1$  was chosen such that it was  $\pi$ -shifting for  $10\ \text{keV}$ . The grating  $G_1$  was fabricated on a  $10\ \mu\text{m}$  polyimide membrane wafer and the  $G_2$  grating on a  $500\ \mu\text{m}$  polyimide wafer.

	Position (mm)	Period ( $\mu\text{m}$ )	Height ( $\mu\text{m}$ )	Material	DC
Target	30				
$G_1$	250	10.6	22	SU8	0.5
$G_2$	448	9.5	70	Gold	0.66
Detector	645				

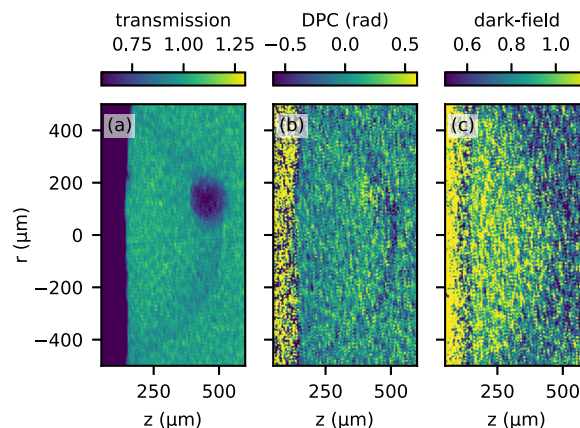


**FIG. 5.** Experimental results from the LULI beamtime: (a) transmission; (b) DPC; (c) dark-field image. The dark spot in the transmission image is a sapphire bead, which will not be discussed in this paper. The highly absorbing vertical area on the left side is a copper flag to shield the detector from preplasma emission.

detector image and a lineout, showing the moiré pattern, are plotted in Figs. 2(b) and 2(d), respectively. With the polyimide wafer for the grating  $G_2$ , we were also able to reduce the number of microfractures to nearly zero, greatly improving the image quality. However, a comparison of the deposited energy in the silicon layer of the JUNGFRÄU detector during both experiments in Figs. 2(a) and 2(b) shows a clear difference in backlighter strength. Normalized to the distance between source and detector, the photon flux of the backlighter X-rays at PHELIX was about six times higher compared with the experiment at LULI. This is most likely due to the small overlap between the  $5\ \mu\text{m}$  backlighter wire and the large focal spot size over which the laser intensity was distributed. The effect of a low backlighter flux can be seen as Poisson noise in the transmission, DPC, and dark-field signals, displayed in Fig. 5. Despite this noise, the shock wave remains distinctly observable within all three image modalities.

These images highlight an additional advantage of grating-based phase-contrast imaging for HED physics. As discussed by Pfeiffer *et al.*,<sup>34</sup> grating-based phase-contrast imaging is capable of measuring the amount of small-angle scattering via the dark-field signal. Employing a low-density foam target with sub-micrometer pore sizes, encased in a Kapton tube of  $1500\ \mu\text{m}$  diameter, resulted in a dark-field signal of  $0.75 \pm 0.03$ , visible in areas unaffected by the

shock wave penetration. However, the signal in the shocked area increased to  $1.03 \pm 0.03$ , indicating a loss of microstructure within the foam. With this successful demonstration of the dark-field's capabilities, it might be the perfect tool for measuring foam homogenization times. Additional applications might be the detection of other small-scale density variations such as turbulence or hydrodynamic instabilities,<sup>10</sup> which can be challenging to detect using conventional radiography.

#### IV. CONCLUSION AND OUTLOOK

Transmission, differential phase-contrast, and dark-field images of laser-driven shock waves in dense matter have been presented. The shock fronts are clearly visible in all three image modalities. A FLASH simulation shows good agreement with the acquired data in the transmission and differential phase-contrast images.

This successful demonstration of grating-based phase-contrast imaging underscores its potential as an additional diagnostic tool in laser plasma physics. Its application is especially interesting in cases where the observed density variations are small, for example when observing the interaction of a shock wave with an object. While we were able to greatly improve our setup between experiments, the results from the beamtime at LULI indicate that the key route to further refinement lies in enhancing the X-ray source flux. A promising technique featuring a small source size and directed X-ray emission might be laser-driven betatron X-ray emission using either gas jets<sup>47</sup> or foam targets.<sup>48</sup> Additionally interesting would be the implementation of grating-based phase-contrast imaging at an X-ray free-electron laser. Using dark-field measurement on shocked plastic foam, we have developed a new plasma diagnostic method that could be useful in measuring the homogenization time of a heated foam target or detecting small-scale density changes such as hydrodynamic instabilities.

#### SUPPLEMENTARY MATERIAL

See [supplementary material](#) for a calibrated spectrum of the tungsten backlighter measured at PHELIX.

#### ACKNOWLEDGMENTS

The results from PHELIX presented here are based on the P-21-00013 experiment performed at the GSI Helmholtzzentrum für Schwerionenforschung, Darmstadt (Germany) in the framework of FAIR Phase-0. The results from LULI presented here are based on the 22PSE1 experiment performed at the École Polytechnique. We would like to give special thanks to the PHELIX and LULI operation teams.

The software used in this work was developed in part by the DOE NNSA- and DOE Office of Science-supported Flash Center for Computational Science at the University of Chicago and the University of Rochester.

The authors acknowledge the support of the Karlsruhe Nano Micro Facility (KNMF), a Helmholtz Research Infrastructure at Karlsruhe Institute of Technology, and microworks GmbH for fabricating the gratings.

This work was funded by the Deutsche Forschungsgemeinschaft (DFG) under Grant No. 452935060 ("Einzelschuss Röntgen-Phasenkontrast Abbildung von dichten Plasmen," <https://gepris.dfg.de/gepris/projekt/452935060>). The experiment at the LULI laser facility was supported by Laserlab-Europe with Grant No. PID20536. The work of A. S. Martynenko was supported by the Alexander von Humboldt Foundation.

#### AUTHOR DECLARATIONS

##### Conflict of Interest

The authors have no conflicts to disclose.

##### Author Contributions

L.W. and S.S. contributed equally to this work.

**Leonard Wegert:** Conceptualization (lead); Data curation (lead); Formal analysis (lead); Investigation (lead); Methodology (lead); Project administration (equal); Resources (lead); Software (lead); Validation (lead); Visualization (lead); Writing – original draft (lead); Writing – review & editing (lead). **Stephan Schreiner:** Conceptualization (lead); Data curation (lead); Formal analysis (lead); Investigation (lead); Methodology (lead); Project administration (lead); Resources (lead); Software (equal); Validation (lead); Visualization (lead); Writing – original draft (lead); Writing – review & editing (lead). **Constantin Rauch:** Conceptualization (lead); Data curation (equal); Formal analysis (supporting); Investigation (equal); Methodology (equal); Project administration (supporting); Resources (equal); Software (lead); Validation (equal); Visualization (supporting); Writing – review & editing (equal). **Bruno Albertazzi:** Data curation (supporting); Investigation (supporting); Methodology (supporting); Project administration (equal); Resources (supporting); Supervision (supporting); Writing – review & editing (supporting). **Paulina Bleuel:** Data curation (supporting); Investigation (supporting); Resources (supporting); Writing – review & editing (supporting). **Eric Fröjdh:** Data curation (supporting); Resources (equal); Software (equal); Supervision (supporting); Writing – review & editing (supporting). **Michel Koenig:** Data curation (supporting); Investigation (supporting); Methodology (supporting); Project administration (equal); Resources (supporting); Supervision (supporting); Writing – review & editing (supporting). **Veronika Ludwig:** Conceptualization (supporting); Funding acquisition (supporting); Resources (supporting); Writing – review & editing (supporting). **Artem S. Martynenko:** Conceptualization (equal); Investigation (equal); Methodology (supporting); Resources (equal); Software (supporting); Visualization (supporting); Writing – review & editing (equal). **Pascal Meyer:** Conceptualization (supporting); Funding acquisition (supporting); Methodology (supporting); Resources (equal); Supervision (supporting); Writing – review & editing (supporting). **Aldo Mozzanica:** Data curation (supporting); Resources (equal); Software (equal); Supervision (supporting); Writing – review & editing (supporting). **Michael Müller:** Data curation (supporting); Investigation (supporting); Resources (supporting); Writing – review & editing (supporting). **Paul Neumayer:** Conceptualization (equal); Data



curation (supporting); Formal analysis (equal); Funding acquisition (lead); Investigation (equal); Methodology (supporting); Resources (equal); Supervision (equal); Validation (supporting); Visualization (supporting); Writing – review & editing (equal). **Markus Schneider:** Data curation (supporting); Investigation (supporting); Methodology (supporting); Resources (equal); Software (supporting); Writing – review & editing (equal). **Angelos Triantafyllidis:** Data curation (supporting); Project administration (supporting); Resources (supporting); Supervision (supporting); Writing – review & editing (supporting). **Bernhard Zielbauer:** Conceptualization (equal); Data curation (supporting); Project administration (equal); Resources (supporting); Writing – review & editing (supporting). **Gisela Anton:** Conceptualization (equal); Funding acquisition (lead); Investigation (equal); Methodology (equal); Project administration (supporting); Supervision (equal); Writing – review & editing (equal). **Thilo Michel:** Conceptualization (equal); Funding acquisition (equal); Investigation (equal); Methodology (equal); Project administration (supporting); Supervision (equal); Writing – review & editing (equal). **Stefan Funk:** Conceptualization (equal); Funding acquisition (lead); Investigation (equal); Methodology (equal); Project administration (lead); Supervision (lead); Writing – review & editing (equal).

## DATA AVAILABILITY

The data that support the findings of this study are available within the article and its [supplementary material](#) and from the corresponding author upon reasonable request.

## REFERENCES

- 1 B. Koziowski, B. Bachmann, A. Do, and R. Tommasini, “X-ray imaging methods for high-energy density physics applications,” *Rev. Sci. Instrum.* **94**, 041102 (2023).
- 2 G. W. Collins, L. B. Da Silva, P. Celliers, D. M. Gold, M. E. Foord, R. J. Wallace, A. Ng, S. V. Weber, K. S. Budil, and R. Cauble, “Measurements of the equation of state of deuterium at the fluid insulator-metal transition,” *Science* **281**, 1178–1181 (1998).
- 3 T. Döppner, D. C. Swift, A. L. Kritcher, B. Bachmann, G. W. Collins, D. A. Chapman, J. Hawrelak, D. Kraus, J. Nilsen, S. Rothman, L. X. Benedict, E. Dewald, D. E. Fratanduono, J. A. Gaffney, S. H. Glenzer, S. Hamel, O. L. Landen, H. J. Lee, S. LePape, T. Ma, M. J. MacDonald, A. G. MacPhee, D. Milathianaki, M. Millot, P. Neumayer, P. A. Sterne, R. Tommasini, and R. W. Falcone, “Absolute equation-of-state measurement for polystyrene from 25 to 60 Mbar using a spherically converging shock wave,” *Phys. Rev. Lett.* **121**, 025001 (2018).
- 4 J. F. Hansen, H. Robey, R. Klein, and A. Miles, “Experiment on the mass stripping of an interstellar cloud following shock passage,” *Astrophys. J.* **662**, 379 (2007).
- 5 G. Rigon, A. Casner, B. Albertazzi, T. Michel, P. Mabey, E. Falize, J. Ballet, L. Van Box Som, S. Pikuz, Y. Sakawa, T. Sano, A. Faenov, T. Pikuz, N. Ozaki, Y. Kuramitsu, M. P. Valdivia, P. Tzeferacos, D. Lamb, and M. Koenig, “Rayleigh-Taylor instability experiments on the LULI2000 laser in scaled conditions for young supernova remnants,” *Phys. Rev. E* **100**, 021201 (2019).
- 6 B. Albertazzi, P. Mabey, T. Michel, G. Rigon, J. R. Marquès, S. Pikuz, S. Ryazantsev, E. Falize, L. Van Box Som, J. Meinecke, N. Ozaki, G. Gregori, and M. Koenig, “Triggering star formation: Experimental compression of a foam ball induced by Taylor–Sedov blast waves,” *Matter Radiat. Extremes* **7**, 036902 (2022).
- 7 M. J.-E. Manuel, B. Khair, G. Rigon, B. Albertazzi, S. R. Klein, F. Kroll, F. E. Brack, T. Michel, P. Mabey, S. Pikuz, J. C. Williams, M. Koenig, A. Casner, and C. C. Kuranz, “On the study of hydrodynamic instabilities in the presence of background magnetic fields in high-energy-density plasmas,” *Matter Radiat. Extremes* **6**, 026904 (2021).
- 8 J. R. Rygg, O. S. Jones, J. E. Field, M. A. Barrios, L. R. Benedetti, G. W. Collins, D. C. Eder, M. J. Edwards, J. L. Kline, J. J. Kroll, O. L. Landen, T. Ma, A. Pak, J. L. Peterson, K. Raman, R. P. J. Town, and D. K. Bradley, “2D x-ray radiography of imploding capsules at the National Ignition Facility,” *Phys. Rev. Lett.* **112**, 195001 (2014).
- 9 D. Paganin, *Coherent X-Ray Optics* (Oxford University Press on Demand, 2006).
- 10 D. Stutman and M. Finkenthal, “Talbot-Lau x-ray interferometry for high energy density plasma diagnostic,” *Rev. Sci. Instrum.* **82**, 113508 (2011).
- 11 A. Schropp, R. Hoppe, V. Meier, J. Patommel, F. Seiboth, Y. Ping, D. G. Hicks, M. A. Beckwith, G. W. Collins, A. Higginbotham, J. S. Wark, H. J. Lee, B. Nagler, E. C. Galtier, B. Arnold, U. Zastra, J. B. Hast-ings, and C. G. Schroer, “Imaging shock waves in diamond with both high temporal and spatial resolution at an XFEL,” *Sci. Rep.* **5**, 11089 (2015).
- 12 D. S. Montgomery, “Invited article: X-ray phase contrast imaging in inertial confinement fusion and high energy density research,” *Rev. Sci. Instrum.* **94**, 021103 (2023).
- 13 J. Workman, J. Cobble, K. Flippo, D. C. Gautier, D. S. Montgomery, and D. T. Offermann, “Phase-contrast imaging using ultrafast x-rays in laser-shocked materials,” *Rev. Sci. Instrum.* **81**, 10E520 (2010).
- 14 L. Antonelli, F. Barbatto, D. Mancelli, J. Trela, G. Zeraouli, G. Boutoux, P. Neumayer, S. Atzeni, A. Schiavi, L. Volpe, V. Bagnoud, C. Brabetz, B. Zielbauer, P. Bradford, N. Woolsey, B. Borm, and D. Batani, “X-ray phase-contrast imaging for laser-induced shock waves,” *Europhys. Lett.* **125**, 35002 (2019).
- 15 F. Pfeiffer, T. Weitkamp, O. Bunk, and C. David, “Phase retrieval and differential phase-contrast imaging with low-brilliance X-ray sources,” *Nat. Phys.* **2**, 258–261 (2006).
- 16 M. P. Valdivia, D. Stutman, C. Stoeckl, W. Theobald, G. W. Collins, V. Bouffetier, M. Vescovi, C. Mileham, I. A. Begishev, S. R. Klein, R. Melean, S. Muller, J. Zou, F. Veloso, A. Casner, F. N. Beg, and S. P. Regan, “Talbot-Lau x-ray deflectometer: Refraction-based HEDP imaging diagnostic,” *Rev. Sci. Instrum.* **92**, 065110 (2021).
- 17 G. Pérez-Callejo, V. Bouffetier, L. Ceurvost, T. Goudal, S. R. Klein, D. Svyatskiy, M. Holec, P. Perez-Martin, K. Falk, A. Casner *et al.*, “Phase imaging of irradiated foils at the OMEGA EP facility using phase-stepping X-ray Talbot-Lau deflectometry,” *High Power Laser Sci. Eng.* **11**, e49 (2023).
- 18 T. Weitkamp, A. Diaz, C. David, F. Pfeiffer, M. Stampanoni, P. Cloetens, and E. Ziegler, “X-ray phase imaging with a grating interferometer,” *Opt. Express* **13**, 6296–6304 (2005).
- 19 M. Schuster, V. Ludwig, B. Akstaller, M. Seifert, A. Wolf, T. Michel, P. Neumayer, S. Funk, and G. Anton, “A fast alignment method for grating-based X-ray phase-contrast imaging systems,” *J. Instrum.* **14**, P08003 (2019).
- 20 B. Akstaller, S. Schreiner, F. Hofmann, P. Meyer, P. Neumayer, M. Schuster, A. Wolf, B. Zielbauer, V. Ludwig, T. Michel, G. Anton, and S. Funk, “Single-shot grating-based phase-contrast imaging of a micrometer sample at a laser-driven x-ray backlighter source,” *J. Instrum.* **16**, P06021 (2021).
- 21 S. Schreiner, B. Akstaller, L. Dietrich, P. Meyer, P. Neumayer, M. Schuster, A. Wolf, B. Zielbauer, V. Ludwig, T. Michel, G. Anton, and S. Funk, “Noise reduction for single-shot grating-based phase-contrast imaging at an X-ray backlighter,” *J. Imaging* **7**, 178 (2021).
- 22 B. Fryxell, K. Olson, P. Ricker, F. X. Timmes, M. Zingale, D. Q. Lamb, P. MacNeice, R. Rosner, J. W. Truran, and H. Tufo, “FLASH: An adaptive mesh hydrodynamics code for modeling astrophysical thermonuclear flashes,” *Astrophys. J., Suppl. Ser.* **131**, 273 (2000).
- 23 S. Schreiner, C. Rauch, B. Akstaller, P. Bleuel, E. Fröjd, A. S. Martynenko, A. Mozzanica, P. Neumayer, L. Wegert, B. Zielbauer *et al.*, “Electromagnetic pulse protective shielding for digital x-ray detectors,” *Rev. Sci. Instrum.* **94**, 075106 (2023).



- <sup>24</sup>A. Momose, S. Kawamoto, I. Koyama, Y. Hamaishi, K. Takai, and Y. Suzuki, "Demonstration of X-ray Talbot interferometry," *Jpn. J. Appl. Phys.* **42**, L866–L868 (2003).
- <sup>25</sup>M. Engelhardt, J. Baumann, M. Schuster, C. Kottler, F. Pfeiffer, O. Bunk, and C. David, "High-resolution differential phase contrast imaging using a magnifying projection geometry with a microfocus x-ray source," *Appl. Phys. Lett.* **90**, 224101 (2007).
- <sup>26</sup>A. Momose, W. Yashiro, H. Maikusa, and Y. Takeda, "High-speed X-ray phase imaging and X-ray phase tomography with Talbot interferometer and white synchrotron radiation," *Opt. Express* **17**, 12540–12545 (2009).
- <sup>27</sup>T. Zhou, U. Lundström, T. Thüning, S. Rutishauser, D. H. Larsson, M. Stampanoni, C. David, H. M. Hertz, and A. Burvall, "Comparison of two x-ray phase-contrast imaging methods with a microfocus source," *Opt. Express* **21**, 30183–30195 (2013).
- <sup>28</sup>A. Mozzanica, A. Bergamaschi, M. Brueckner, S. Cartier, R. Dinapoli, D. Greiffenberg, J. Jungmann-Smith, D. Maliakal, D. Mezza, M. Ramilli *et al.*, "Characterization results of the JUNGFRÄU full scale readout ASIC," *J. Instrum.* **11**, C02047 (2016).
- <sup>29</sup>F. Consoli, V. T. Tikhonchuk, M. Bardoni, P. Bradford, D. C. Carroll, J. Cikhart, M. Cipriani, R. J. Clarke, T. E. Cowan, C. N. Danson *et al.*, "Laser produced electromagnetic pulses: Generation, detection and mitigation," *High Power Laser Sci. Eng.* **8**, e22 (2020).
- <sup>30</sup>P. Meyer, T. Beckenbach, F. An, T. Schröter, J. Schulz, and J. Mohr, "X-ray gratings for grating-based x-ray DPCI fabricated using the deep x-ray lithography process: State of the art," in *XNPIG Conference Proceedings* (ETH Zurich, Zurich, Switzerland, 2017), pp. 110–111.
- <sup>31</sup>H. F. Talbot, "Facts relating to optical science," *Philos. Mag.* **9**, 401–407 (1836).
- <sup>32</sup>T. J. Suleski, "Generation of Lohmann images from binary-phase Talbot array illuminators," *Appl. Opt.* **36**, 4686–4691 (1997).
- <sup>33</sup>I. Amidror, *The Theory of the Moiré Phenomenon* (Springer Verlag GmbH, 2009).
- <sup>34</sup>F. Pfeiffer, M. Bech, O. Bunk, P. Kraft, E. F. Eikenberry, C. Brönnimann, C. Grünzweig, and C. David, "Hard-X-ray dark-field imaging using a grating interferometer," *Nat. Mater.* **7**, 134–137 (2008).
- <sup>35</sup>M. Takeda, H. Ina, and S. Kobayashi, "Fourier-transform method of fringe-pattern analysis for computer-based topography and interferometry," *J. Opt. Soc. Am.* **72**, 156–160 (1982).
- <sup>36</sup>E. E. Bennett, R. Kopace, A. F. Stein, and H. Wen, "A grating-based single-shot x-ray phase contrast and diffraction method for in vivo imaging," *Med. Phys.* **37**, 6047–6054 (2010).
- <sup>37</sup>M. Seifert, M. Gallersdörfer, V. Ludwig, M. Schuster, F. Horn, G. Pelzer, J. Rieger, T. Michel, and G. Anton, "Improved reconstruction technique for moiré imaging using an X-ray phase-contrast Talbot–Lau interferometer," *J. Imaging* **4**, 62 (2018).
- <sup>38</sup>P. Modregger, B. Pinzer, T. Thüning, S. Rutishauser, C. David, and M. Stampanoni, "Sensitivity of X-ray grating interferometry," *Opt. Express* **19**, 18324–18338 (2011).
- <sup>39</sup>T. Thüering and M. Stampanoni, "Performance and optimization of X-ray grating interferometry," *Philos. Trans. R. Soc., A* **372**, 20130027 (2014).
- <sup>40</sup>S. Schreiner, C. Rauch, B. Akstaller, P. Bleuel, E. Fröjd, V. Ludwig, A. Martynenko, P. Meyer, A. Mozzanica, M. Müller, P. Neumayer, M. Schuster, L. Wegert, B. Zielbauer, A. Wolf, G. Anton, T. Michel, and S. Funk, "Design of a Talbot phase-contrast microscopy imaging system with a digital detector for laser-driven X-ray backlighter sources," *J. Instrum.* **19**, P05004 (2024).
- <sup>41</sup>B. Borm, D. Khaghani, and P. Neumayer, "Properties of laser-driven hard x-ray sources over a wide range of laser intensities," *Phys. Plasmas* **26**, 023109 (2019).
- <sup>42</sup>V. Bagnoud, B. Aurand, A. Blazevic, S. Borneis, C. Bruske, B. Ecker, U. Eisenbarth, J. Fils, A. Frank, E. Gaul, S. Goette, C. Haefner, T. Hahn, K. Harres, H.-M. Heuck, D. Hochhaus, D. H. H. Hoffmann, D. Javorková, H.-J. Kluge, T. Kuehl, S. Kunzer, M. Kreutz, T. Merz-Mantwill, P. Neumayer, E. Onkels, D. Reemts, O. Rosmej, M. Roth, T. Stoehlker, A. Tauschwitz, B. Zielbauer, D. Zimmer, and K. Witte, "Commissioning and early experiments of the PHELIX facility," *Appl. Phys. B* **100**, 137–150 (2010).
- <sup>43</sup>LANL, "SESAME: The Los Alamos National Laboratory equation of state database," Report No. LA-UR-92-407, 1979.
- <sup>44</sup>N. H. Magee, J. Abdallah, R. E. H. Clark, J. S. Cohen, L. A. Collins, G. Csanak, C. J. Fontes, A. Gauger, J. J. Keady, D. P. Kilcrease, and A. L. Merts, "Atomic structure calculations and new LOS Alamos astrophysical opacities," in *Astrophysical Applications of Powerful New Databases*, edited by S. J. Adelman and W. L. Wiese (Astronomical Society of the Pacific, 1995), Vol. 78, p. 51.
- <sup>45</sup>W. L. Kruer, "Intense laser plasma interactions: From Janus to Nova," *Phys. Fluids B* **3**(8), 2356–2366 (1991).
- <sup>46</sup>A. Wolf, "X-ray microscopy and phase imaging towards time-resolved applications in laboratory astrophysics," Ph.D. thesis, Friedrich-Alexander-Universität Erlangen-Nürnberg, 2022, available at <https://nbn-resolving.org/urn:nbn:de:bvb:29-opus4-199184>.
- <sup>47</sup>F. Albert, N. Lemos, J. L. Shaw, P. M. King, B. B. Pollock, C. Goyon, W. Schumaker, A. M. Saunders, K. A. Marsh, A. Pak, J. E. Ralph, J. L. Martins, L. D. Amorim, R. W. Falcone, S. H. Glenzer, J. D. Moody, and C. Joshi, "Betatron x-ray radiation from laser-plasma accelerators driven by femtosecond and picosecond laser systems," *Phys. Plasmas* **25**, 056706 (2018).
- <sup>48</sup>O. N. Rosmej, X. F. Shen, A. Pukhov, L. Antonelli, F. Barbato, M. Gyrdymov, M. M. Günther, S. Zähter, V. S. Popov, N. G. Borisenko, and N. E. Andreev, "Bright betatron radiation from direct-laser-accelerated electrons at moderate relativistic laser intensity," *Matter Radiat. Extremes* **6**, 048401 (2021).